Characterization of morphology in ring-opening metathesis polymerized novel solid block copolymer electrolytes by atomic force microscopy and X-ray scattering

Megan Longstaff, Kaitlin Gardiner, Rodion Zhuravlev, Jacob Finney[1], and Dean A. Waldow[*]

Department of Chemistry, Pacific Lutheran University, Tacoma, WA 98447 USA

ABSTRACT

Block copolymers present the ability to design solid polymer electrolytes to include both ion conductivity and structural features which may lead to improved safety in lithium ion batteries. We report a morphology study of novel block copolymer electrolytes that were synthesized using ring opening metathesis polymerization. The monomers have an oxanorbornene dicarboximide backbone where the first block has oligomeric (n=12) ethylene oxide (OEO) side chains and the second block has phenyl side groups. The former block achieves high salt solubility, while the latter block is a structural component with a high glass transition temperature. Block copolymers have been synthesized covering a range of compositions from 38 to 70 wt % of the phenyl containing block, and have been studied neat and with bis(trifluoromethane)sulfonimide lithium salt. The resulting morphologies were investigated using atomic force microscopy and small angle X-ray scattering (SAXS). Solvent vapor annealing was found to enhance ordering in the neat copolymer thin films and the addition of salt with solvent vapor annealing further increased long range order. Cylinder and lamellar structures dominate the observed morphologies and the addition of salt increases ordering and the range block copolymer compositions with lamellar structure. SAXS results demonstrate modest ordering, reinforce the observations from AFM, and show an increase in domain size with an increase in salt concentration.

[*] Corresponding author: Tel. 1-253-535-7533; E-mail address: waldowda@plu.edu
[1] Present address: Department of Chemistry, University of Washington, Seattle, WA 98195; E-mail address: finneyjm@uw.edu

1. Introduction

Various forms of energy storage including fuel cells, batteries, and supercapacitors depend on effective transport of ions for their function as well as other applications of ion transport, and research into these areas is of continued interest [1-3]. Small molecule organic based electrolytes such as organic carbonates are still of significant commercial importance primarily due to their excellent ion conductivity. These flammable liquid organic electrolytes cannot alone resist the growth of metal dendrites which can occur in lithium related batteries. As a result, an electrical short can develop possible leading to failures and safety concerns including fires [1, 4, 5]. Changing the flammable fluid organic electrolyte to a solid polymer electrolyte (SPE) will greatly reduce the flammability of the electrolyte. Poly(ethylene oxide) (PEO) was one of the earliest SPEs developed[6] and continues to be a standard to which other SPEs are compared [7]. PEO does achieve high lithium salt solubility, improved fire safety, and high conductivity at elevated temperature (10^{-3} S/cm at ~ 80 °C). Despite these important benefits, PEO [8] at ambient operating temperatures has low conductivity, can crystallize, has a low transference number, and has a low mechanical modulus [9]. Many alternative chemical structures have been investigated for SPEs as well with varied successes [10-14]. Dendrites can be suppressed with the use of a high mechanical modulus electrolyte though such SPEs with sufficient conductivity has largely remain elusive [1, 5, 15, 16].

In SPEs, ion motion is thought to be chiefly connected with the segmental motion of a polymer backbone allowing for ion motion on that timescale [17] and illuminates PEO's conductivity due to its low glass transition temperature. Sokolov and coworkers have taken an alternative approach in addressing this issue by attempting to decouple segmental motion from ion conductivity [18-24]. They design polymers that have frustrated chain packing which can allow for ion motion to be faster than segmental motion. Current glass transition theory suggests that frustrated chain packing should increase with polymer fragility [9, 25]. Decoupling of segmental motion from ion conductivity has been demonstrated along with an increase in conductivity with increased polymer fragility[18, 22, 26]. Recent conductivity studies for a novel polymer electrolyte based on a bulky polymer backbone and shorter ethylene oxide (EO) side chains also demonstrated significant decoupling but at the expense of an increased glass temperature [27] while longer EO side chains had less decoupling.

Even if an SPE can achieve the desired conductivity similar to that of liquid electrolytes, it is not

likely to have a large mechanic modulus. This concern has led to research into building an SPE with the dual qualities of facile conductivity and large mechanical modulus in one material through the use of block copolymers [28] with their associated phase separated morphologies effectively combining both properties into one material [29, 30]. Balsara and coworkers extensively studied polystyrene-block-poly(ethylene oxide) (SEO) copolymer in addition to other groups [16, 31-36]. Yuan and co-workers[31] found that for SEO block copolymers with salt the PS block at higher molecular weight had a glass transition temperature of ~100 °C and the PEO block had a glass temperature of approximately -40 °C. Other types of block copolymers have also been investigated [29, 30, 37, 38]. Gai and coworkers recently studied the morphologies of a bottlebrush block copolymer with a norbornene backbone and block of side chain polystyrene and a block of side chain poly(ethylene oxide) [39].

In this research, we present results for a novel diblock copolymer where the ion conductive block is similar to the previous research though a longer oligomeric ethylene oxide (OEO) side chain and the structural block uses the same backbone structure but with a phenyl side group which has a high glass transition temperature. This current research builds on our previous homopolymer results [27] which demonstrated decoupling of segmental motion from conductivity with the use of a bulky oxanorbornene dicarboximide backbone and shorter OEO side chains (2-4 EO units). The polymers with a longer OEO side chain (8 EO units) had reduced decoupling but higher conductivity. The block copolymers are synthesized using ring opening metathesis polymerization with a wide range of block compositions from 0.38 to 0.70 weight fraction of the structural block. The morphologies developed have been studied both as neat samples as well as with lithium bis(trifluoromethane)sulfonimide lithium (LiTFSI) salt using atomic force microscopy and X-ray scattering. Cylindrical and lamellar structures constitute the majority of morphologies observed. Vapor annealing techniques are used in sample preparation to better order the materials.
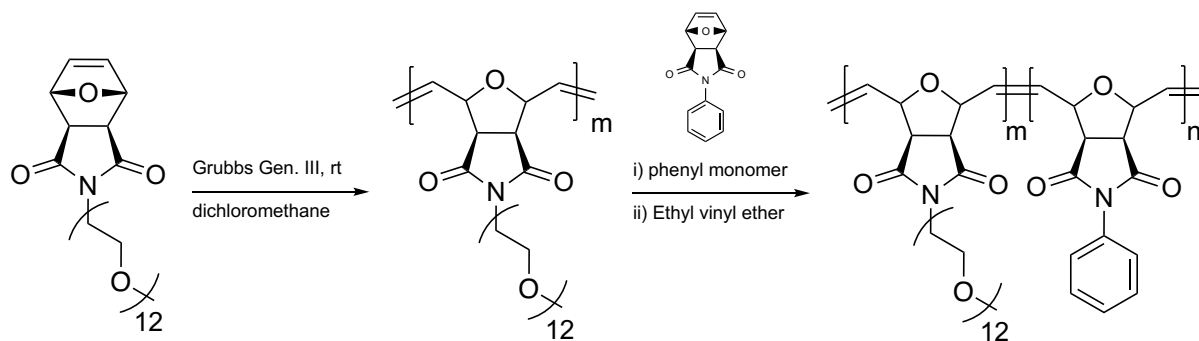
2. Experimental

2.1. Synthesis of monomers and polymers

All chemicals used are the same as previously reported[27] with the addition of phenylmaleimide (TCI America) and methoxypolyethylene glycol 550 (Sigma-Aldrich) which were also used as received. The synthesis of the monomers is identical to those procedures previously published with the following differences. For the salt soluble monomer (ONDI-12), a side chain of oligomeric ethylene oxide (OEO) with an average of about 12 units was attached to

oxanorbornenedicarboximide (ONDI) in the same fashion as ONDI-8 from the reference above using a Diels-Alder reaction followed by alkylation with the tosyl functionalized OEO. The structural monomer, phenyloxynorbornenedicarboximide (ONDI-ph), was synthesized following the ONDI protocol substituting phenylmaleimide instead of maleimide. Both monomers were characterized using proton NMR and had exo content exceeding 99%. All ROMP polymerizations were carried out using a third generation Grubbs catalyst under an argon atmosphere. Four poly(ONDI-12) homopolymers were synthesized for conductivity studies with degrees of polymerization ranging from ~ 60 to 370. Multiple poly(ONDI-12-*block*-ONDI-ph) copolymers were synthesized (Scheme 1) in the same manner except the ONDI-ph block was added after 30 minutes and allowed to react for an additional 30 minutes before terminating the reaction with ethylvinylether. The copolymers were purified via precipitation into either methanol or diethylether. Proton NMR spectra of intermediates and products (Appendix A) were collected with a 500 MHz Bruker Avance III spectrometer and used to characterize the products. All diblock copolymers were synthesized for a total molecular weight of ~60 kDa with varying block compositions subsequently measured by NMR as described in Table 1.

Scheme 1. General diblock copolymer synthesis scheme.

2.2. Electrochemical impedance spectroscopy measurements

Electrochemical impedance spectroscopy (EIS) was performed using a Gamry Reference 600+ potentiostat to determine the side chain length with the best conductivity at room temperature prior synthesizing the block copolymers. A solution was made using ~20 mg of homopolymer and ~ 10 mg of LiTFSI in 0.5 mL of THF to give a homogenous sample with 33 wt % salt post solvent evaporation. Aliquots of this solution were drop cast on to a gold coated brass electrode under argon flow that had been cleaned with acetone and then with a Harrick Plasma PDC-32G Plasma Cleaner. Each sample was put under active vacuum for 24 hours and then heated to 70 °C for four

hours. The sample was transferred to a nitrogen glovebox (water and oxygen < 0.1 ppm), and the cell was assembled with a Teflon spacer (0.005") between the electrodes. EIS spectroscopy was performed over a frequency range of 0.1 Hz to 5 MHz under nitrogen. The sample was initially annealed at 80°C for an hour and then EIS data was measured at 5° C increments (± 0.1 °C) down to room temperature allowing 20 minutes of annealing once reaching each controlled temperature. The electrode area coverage was measured at the end of the measurements. Conductivity was calculated using $\sigma = L/RA$ where the A is the measured sample area in contact with the electrode, L is the thickness of the spacer, and R is the measured impedance from the minimum of a Nyquist plot.

2.3. Atomic force microscopy measurements

AFM experiments were performed using an Asylum Research MFP-3D atomic force microscope in AC Topography / tapping mode. AFM cantilevers used in imaging were either Budget Sensors Tap300g, Oxford Instruments HQ-75-Au, or Oxford Instruments HQ-300-Au cantilevers with typical tip radii of curvatures of about 10 nm. Samples for AFM were prepared on coverslips that were cleaned with isopropanol with subsequent plasma cleaning or using an acid bath. Polymer solutions (180 µL of ~2.0 wt %) were spun cast under a nitrogen atmosphere (500 rpm for 5 s, then 2000 rpm for 60 s) and resulted in ~150 nm thick films. For solvent annealing, a sample was placed in an argon filled 270 mL jar away from direct solvent contact. Dichloromethane (0.5 mL) was added to the bottom of the jar and capped tightly for ~ 60 to 75 minutes. After solvent vapor annealing, the sample was placed in an active vacuum to remove residual solvent vapor prior to imaging.

2.4. SAXS measurements

SAXS data were collected using beamline 12-ID-B at the X-ray Science Division beamlines at the Advanced Photon Source, Argonne National Laboratory. All SAXS samples were annealed using a slow solvent evaporation (SSE) method[40] under argon and on Teflon substrates, and solvent annealed for approximately two days followed by two days under active vacuum. During SAXS measurements, the samples were housed in DSC pans and suspended in a temperature controlled (40 °C) sample holder using Kapton tape. All samples were stored under nitrogen until measured.

2.5. DSC measurements

Differential scanning calorimetry (DSC) measurements were conducted using a Perkin-Elmer Pyris 1 instrument for some of the neat block copolymers. The glass transition temperature was measured during the second cycle (heating and cooling rates were 10 °C/min.). The transition temperature was taken as the midpoint of the specific heat step for observed transitions. Evidence of crystallization was not detected in any of the samples.

Table 1. The block copolymers used in this study are given with the weight fraction of phenyl monomer content. All samples were studied with AFM and the samples with SAXS data and measured glass transition temperatures are indicated.

Sample	ONDI-ph wt. frac.	T_g °C (OEO)	T_g °C(P)	SAXS
P-38	0.38	-55	185	✓
P-47	0.47	a	a	a
P-48	0.48	-53	181	✓
P-58	0.58	-55	176	✓
P-61	0.61	a	a	a
P-70	0.70	-52	b	✓

a: not acquired, b: indeterminate, ✓: acquired

3. Results and Discussion

3.1. Design and characterization of block copolymers

Homopolymer ion conductivity data was used to decide on the block copolymer used in this research. Results from Adams, et al. [27] demonstrated for a homopolymer with an oxynorbornenedicarboximide backbone with OEO side chains the level of decoupling increased and in addition the glass transition temperature also increased negating some of the gains. The homopolymers with fastest ion conductivity had an OEO side chain of length of 8 but less decoupling. Increased conductivity was desired so additional homopolymers were synthesized with an average OEO side chain length of ~12 and at varying degrees of polymerization. The measured glass transition temperatures for this polymer were -59 °C neat and -24 °C with 33 wt % LiTFSI. EIS was used to measure conductivity for the poly(ONDI-12) homopolymers with 33 wt % LiTFSI. All samples exhibited temperature dependent conductivity that follows typical Vogel-Fulcher-Tammann (VFT) behavior [11, 12] as described by Eq. 1.

$$\sigma = \sigma_0 exp\left(-\frac{B}{T-T_0}\right) \tag{1}$$

The log of conductivity versus inverse temperature is presented in Fig. 1 for a poly(ONDI-12) homopolymer (DP = 62) at temperatures from 80 °C to 25 °C. The data in Fig. 1 was fit using Eq. 1 as seen by the solid line with B = 1230 K and T_o = 199 K. It was found that conductivity was not a function of the degree of polymerization for the poly(ONDI-12) homopolymers that were synthesized. At 25 °C, conductivity was found to have an average value of (1.6 ± 0.4) x 10^{-6} S/cm and reaches a notable conductivity of ~1×10^{-4} S/cm at 80 °C. The conductivity at 25 °C is about an order of magnitude higher than the highest conductivity of the related ONDI homopolymer, poly(ONDI-8), previously reported for this class of homopolymers [27]. This improvement in conductivity is presumably due the glass transition temperature of this poly(ONDI-12) polymer allowing more motion of the ions. Given this result, block copolymers were synthesized as described in the experimental section using the ONDI-12 monomer (OEO side chain with a length of 12) for the ion soluble block and an ONDI-ph monomer as the structural block with compositions given in Table 1.

One measure of the level of block segregation is the demonstration of a glass transition temperature for each block. The glass transition temperatures were measured for the homopolymers and a sampling of the block copolymers. The Tg of poly(ONDI-ph) and poly(ONDI-12) homopolymers were found to 223 °C and -58 °C respectively. Block copolymers P-38, P-48, and P-58 all demonstrated two consistent glass transition temperatures where the ONDI-ph block average Tg was 180 ± 6 °C and the ONDI-12 block Tg was -55 ± 3 °C. These results are consistent with phase separated morphology and suggests a good potential for developing longer range ordering which would benefit ion mobility in this dual-purpose solid polymer electrolyte.

3.2. Nanomorphology of neat block polymers

These diblock copolymers do not have a known Flory-Huggins interaction parameter (χ) though the development of block copolymer morphologies is suggested by the DSC shown in Table 1. All AFM images presented have a lateral image size of 2 μm by 2 μm, and the scalebar size in the image is 400 nm. Consistent with the DSC results, AFM data did not demonstrate evidence of crystalline ordering but only regions of block copolymer domain ordering. Initially, AFM height images were studied for pure block copolymers spun cast without subsequent treatment. Fig. 2a shows an example height AFM image for sample P-51 spun cast to a thickness of ~150 nm. The vertical relief of this image covers a range of about 10 nm and is typical of the

images presented. There is some observable domain ordering demonstrated in this image. Longer range order is desirable to allow domain interconnectivity for effective ion transport. To improve ordering, solvent vapor annealing (SVA) was employed where the copolymer film was placed in a container with a controlled amount of solvent vapor and allowed to anneal for a period of time. The vapor dissolves in the film effectively lowering the glass transition temperature which allows more polymer motion often leading to increased ordering. Afterward, remaining dissolved vapor was removed with vacuum. Fig. 2b shows the same P-51 sample after SVA in dichloromethane vapor for 70 minutes. The improvement in ordering is dramatic and the image appears to show characteristic lamellar type structure oriented perpendicular to the surface.

Diblock copolymers were then spun cast onto glass coverslips, solvent vapor annealed with dichloromethane, and imaged by AFM in tapping mode. The resulting images for samples P-38, P-47, P-48, P-58, P-61, and P-70 are presented in Fig. 3. The ONDI-ph block weight fractions of these sample range from 0.38 to 0.70. For all AFM images, the false color scale indicates relative height where yellow is high and black is low. The height topography of the domains observed cover approximately 10 nm from the top to bottom of a domain feature excluding larger scale surface roughness. The high areas are rich in the ONDI-ph block and the low areas are rich in ONDI-12 block. This was determined from the portion of low area for high weight fraction ONDI-12 (P-38) and the complementary observation at high ONDI-ph block where the high regions dominate. This observation has also been corroborated by infrared photoinduced force microscopy (PiFM) which can image based on a particular vibrational frequency allowing for the chemical identification of different topographies [41]. The morphology for both samples P-38 (a) and P-70 (f) show cylinders apparently oriented perpendicular to the surface. The former image shows a higher degree of order with even some hexagonal packing regions, while the latter image shows some cylinders at different orientations indicating less order. Samples P-58 (d) and P-61 (e) both appear to demonstrate a lamellar morphology perpendicular to the surface. If the lamellae were parallel to the surface, they would image as a flat surface. The last two images, P-47 (b) and P-48 (c), both appear to be in transition from cylinders to towards lamellae as one would expect with the former showing what appear to be more disordered cylinders with short range order despite the SVA. The latter image appears to show significantly better order with what appears to domains of cylinders and other areas appear more lamellae-like.

Four of the copolymers have been also studied by SAXS. Fig. 4 shows SAXS scattering

data for neat samples of P-38, P-48, P-58, and P-70 plotted in a Kratky style format as log(Iq^2) versus q where q is the scattering angle ($q = 4\pi \sin(\theta/2)/\lambda$). The sample preparation for SAXS was similar to AFM in that the samples were annealed in dichloromethane vapor but with a slow solvent evaporation technique [40] which was necessary for morphologies to develop in these bulk samples. The four data sets have been vertically offset for clarity. The data clearly show peaks which are associated with the types of periodic structures present in the samples, however, the peaks are noticeably broad indicating moderate ordering. These peak positions are analyzed relative to the dominant low q peak referred to as q*. Two common structures are lamellae and hexagonally packed cylinders which have q/q* ratios of 1, 2, 3, … and 1, √3, 2, √7..., respectively. These are the two most notably structures that appear in the AFM images. AFM data for sample P-38 suggests that the sample has formed cylindrical domains and so the data in Fig. 4 is labeled with those values at the q locations relative to q*, e.g., √3q*. The second and third peaks for a cylinder structure (√3q*, 2q*) are encompassed by a broad peak and a very weak 3q* peak is also seen. The scattering data for P-48 is similar to P-38 in peak breadth and relative locations, however, the peaks are at lower absolute q indicating a larger domain size where the size is inversely related to q* through the equation, $d = 2\pi/q^*$. The P-58 sample demonstrates slightly smaller sizes (larger q*) with notably peaks at 1q*, 2q*, and 3q*. Additionally, it appears that there is also scattering between the first two peaks with a shoulder on the high q side of q* and a broad in between q* and 2q* peaks. This additional scattering is consistent with cubic gyroid ratios of $(4/3)^{1/2}$q*, $(7/3)^{1/2}$q*, and $(8/3)^{1/2}$q* (shown as upward pointing arrows in between q* and 2q* peaks in Fig. 4). However, individual peaks are not resolved due to the broad scattering data. It is plausible that this sample has a mixture of gyroid and lamellar regions but lamellae are only seen in the AFM image. The last set of data for P-70 also is similar to the first two sets of data suggesting a cylindrical structure consistent with AFM data. The SAXS results for the bulk prepared samples show only moderate ordering even with the use of the SSE annealing method compared to significant ordering seen in the thin-film AFM samples annealed by SVA. Overall, the SAXS data are consistent with the AFM data suggesting a lamellar region samples P-58 and P-61 aside from the potential gyroid peaks seen for P-58 from SAXS data where only lamellae are observed in the AFM data.

3.3. Nanomorphology of block polymers with added LiTFSI

The same diblock copolymers were now prepared with LiTFSI salt at 33 wt % relative to

the ONDI-12 ion soluble portion of the block composition and were spun cast onto glass coverslips, solvent vapor annealed, and imaged by AFM. The height images for samples P-38, P-47, P-48, P-58, P-61, and P-70 with LiTFSI are presented in Fig. 5. The addition of LiTFSI has increased the ordering compared to the bulk samples in Fig. 3 which is consistent with the salt dissolving in the ONDI-12 block preferentially and resulting in an increase in the Fory-Huggins parameter (χ) leading to better separation of the blocks. For P-38, the observed structure appears to show cylinders, however, they appear mostly parallel with the surface though there are still small regions of cylinders oriented perpendicular to the surface. The image for P-70 was much more difficult to image as seen in the diffuse regions of the image but it also appears to demonstrate cylinders parallel to the surface in areas of better order. Sample P-47 is much more ordered compared to its image without salt and appears to be in transition between cylinders and lamellae but not clearly showing a gyroid structure either. In contrast, samples P-48, P-58, and P-61 all appear to have lamellae perpendicular to the surface with P-58 showing the most significant ordering. The two main conclusions from the samples with added LiTFSI are that the salt noticeably increases the order in all samples and they show a wider weight fraction region with lamellar structures.

Fig. 6 shows SAXS scattering data for samples P-38, P-48, P-58, and P-70 with ~39 wt % LiTFSI relative to the ONDI-12 ion soluble portion of the copolymer. The samples are prepared using slow solvent evaporation, and the SAXS scattering data are again plotted in a Kratky style format. The data sets have been vertically offset for clarity. The peaks observed are still noticeably broad – similar to those in Fig. 4. Two anticipated structures are lamellae and cylinders from the AFM data in Fig. 5. Height AFM data for sample P-38 from Fig. 5 suggests the sample has formed cylindrical structures and the data in Fig. 6 is labeled with those values at the q locations. Again, the second and third peaks for a cylinder structure ($\sqrt{3}q^*$, $2q^*$) appear encompassed by a broad peak and a very weak $3q^*$ peak is seen. The scattering data for P-48 does not show any peaks in contrast to all other scattering data which could be due to either the sample being disordered or having lamellae perpendicular to the beam direction. The latter explanation is consistent with lamellae formation seen in the AFM data of Fig. 5. The P-58 sample demonstrates clear lamellae peaks at $1q^*$, $2q^*$, and $3q^*$. The scattering between the first two peaks seen in the data presented in Fig. 4 for the bulk state is gone. The data for P-70 shows one dominant peak suggesting only weak ordering and is consistent with the difficulty seen in developing order in the AFM data.

Again, these results highlight the difficulty in developing long range order and is most notable in the bulk prepared SAXS samples compared to SVA prepared ~150 nm thick AFM samples. Overall, the SAXS data in Fig. 6 are consistent with the AFM data in Fig. 5 and the data suggest a wider lamellar region encompassing samples P-48, P-58, and P-61.

Samples P-38, P-48, and P-58 were also studied only by SAXS at higher salt concentrations of 56 wt %, 50 wt %, and 46 wt %, respectively, relative to the ONDI-12 portion of the block copolymer composition. The P-70 sample was beyond saturation at these concentrations and was not included. The SAXS data for these three samples are presented in Fig. 7 where the curves are vertically offset for clarity. All q* peaks occur at smaller q values than the lower salt concentration data indicating larger domains at this higher salt concentration. The P-38 data continues to suggest a cylinder morphology with very similar data to the lower concentration sample. The P-48 data shows a low q* peak in contrast to the lower concentration data where no peaks were seen, however, without higher q peaks the structure cannot be assigned. Lastly, the P-58 data appears to be developing a cylindrical structure with weak peaks at √3q* and √7q*. The ability of these diblock copolymers to dissolve LiTFSI ~50 wt % in the ONDI-12 block is notable. Fig. 8 plots the real space dimension ($d = 2\pi/q^*$) of the q* peaks for samples P-38, P-48, and P-58 as a function of weight percent of added LiTFSI. All block copolymers show a substantial increase in domain size with added LiTFSI salt. This is presumably due to the salt preferentially swelling the ONI-12 block thus increasing it volume relative to the ONDI-ph block. It is notable that the P-48 sample demonstrated the largest real space domain sizes likely due to the weight fraction being close to 50%.

Chu and coworkers [12] have studied SPEs with similar side groups with a more flexible ethylene backbone (ATRP synthesis) where their copolymers have an oligomeric ethylene oxide side chain in one block and a polystyrene for the other block. Their focus was on tapering effects between blocks. They found lamellar morphology for the non-tapered block that transitioned to cylindrical morphology with added salt. Simulations performed by Chu and coworkers [42] using a bead-spring model of PS-PEO block copolymer with ions modeled as beads is of interest to our results. They examined the phase diagram of the simulated block copolymer neat and with salt. Two of their three main conclusions are consistent with our results. They report that the range of copolymer compositions for ordered phases increases with added salt and our data indicates a

wider range of copolymer compositions that have lamellae morphology with LiTFSI. Secondly, they report shift of copolymer morphologies towards the PS rich composition side of their phase diagram and is consistent with our observations that lamellae formation dominant at higher ONDI-ph block weight fractions. The last conclusion they reported was a decrease in value of $(\chi N)_{ODT}$ which was not measured in this research.

4. Conclusion

We have synthesized novel block copolymers that include both an ion conductive block and a structural block. Their morphologies have been investigated using AFM and SAXS both in a neat state as well as with LiTFSI. The block copolymers were found to have high salt solubility (up to ~50 wt %) relative to the ONDI-12 block for some copolymer weight fractions. Both neat copolymers and copolymers with LiTFSI were able to develop significantly ordered structures, however, solvent vapor annealing was key to develop longer range ordering. Block copolymers with both LiTFSI and SVA had increased ordering compared to only SVA. The morphologies observed primarily included cylinders and lamellae with a wider weight fraction region of lamellar structures in the AFM samples with ~33 wt % LiTFSI. The domain sizes as measured from the q* peaks in SAXS show increased domain sizes with increased LiTFSI concentration. These results set the stage for EIS measurements to correlate the morphologies and level of ordering with ion conductivity in order to retain as much of the homopolymer conductivity while including a structural component for potential dendrite protection. The required use of vapor phase annealing to produce ordered structures in these block copolymer samples suggests the potential need to increase the Flory-Huggins parameter, χ, or increase the copolymer molecular weight as these might allow more facile morphology development.

Figures:

Fig. 1. Conductivity was measured by electrochemical impendence spectroscopy and is shown for a poly(ONDI-12) homopolymer with ~33 wt % LiTFSI. The log of conductivity is plotted versus inverse temperature and covers a temperature range from 80 °C to 25 °C. The solid line running through the data points is a VFT fit.
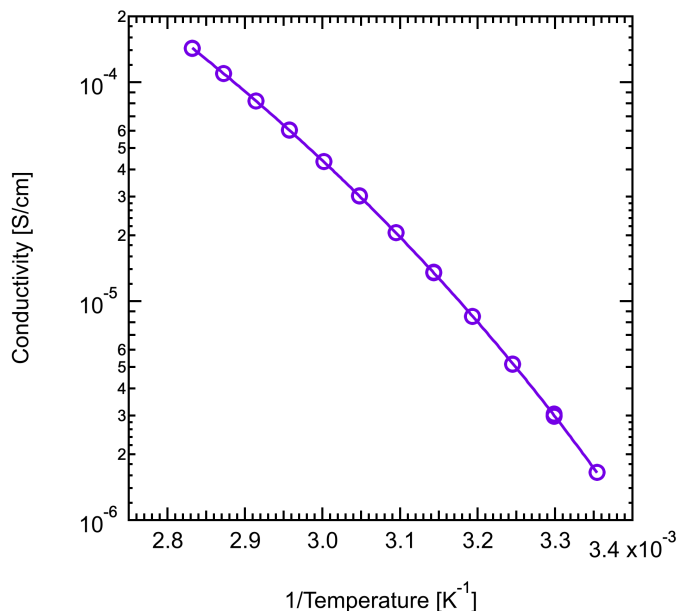

Fig. 2. AFM height images (2 µm x 2 µm) are presented for a sample of neat P-61 both pre (a) and post (b) solvent vapor annealing with dichloromethane. Yellow denotes higher regions while black denotes lower regions. The height difference in domains are on the order of 10 nm. The scale bar is 400 nm.

13

Fig. 3. AFM height images (2 μm x 2 μm) are presented for six neat copolymer films covering a range in ONDI-ph block weight fraction from 0.38 to 070. All spun cast samples have been solvent vapor annealed. The scale bar is 400 nm. The samples include: P-38 (a), P-47 (b), P-48 (c), P-58 (d), P-61 (e), and P-70 (f).
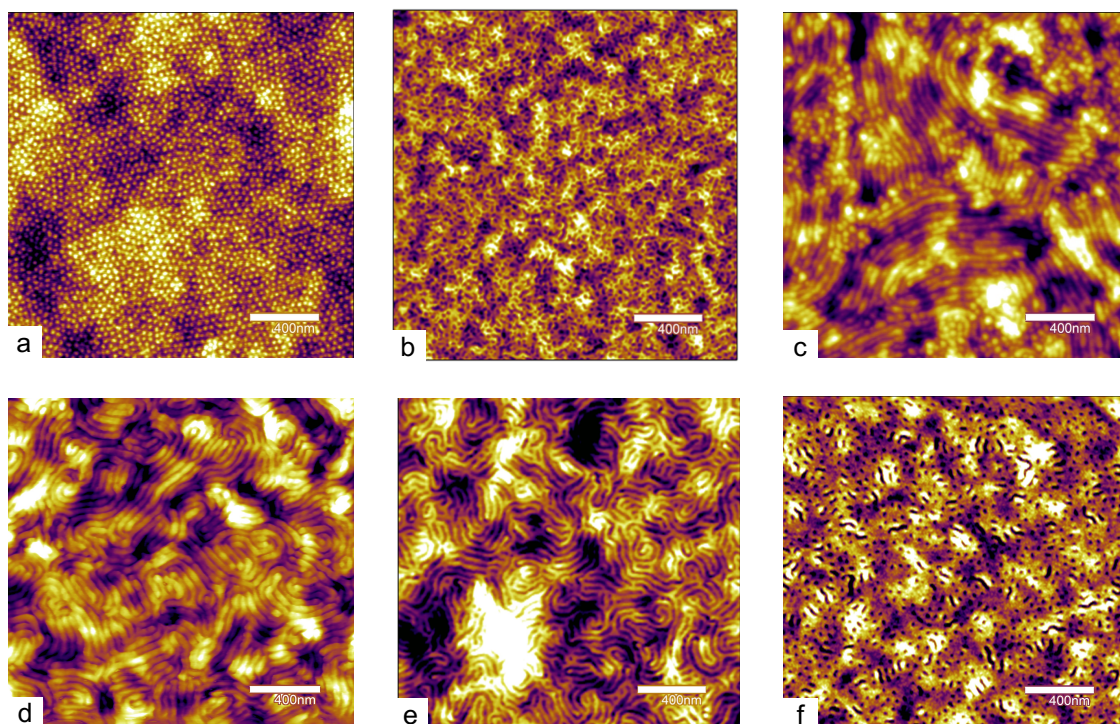
Fig. 4. SAXS data is presented for four neat bulk polymer samples including P-38, P-48, P-58, and P-70. Scattering data is plotted in a Kratky format ($\log(Iq^2)$ vs q) to emphasize the peaks. The numerical labels on each data set indicate the anticipated $q/q*$ ratios from observed morphology via AFM except for P-58 which includes upward facing arrows indicating potential gyroid peak ratios[43] of $(4/3)^{1/2}$, $(7/3)^{1/2}$, and $(8/3)^{1/2}$ in order from left to right.
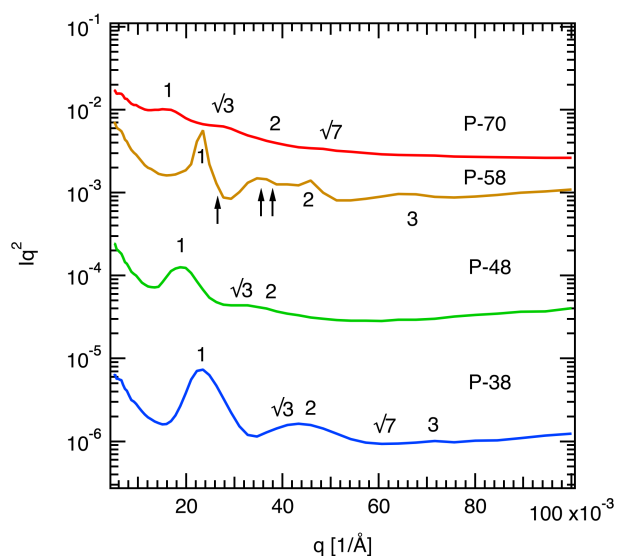
Fig. 5. AFM height images (2 µm x 2 µm) are presented for six polymer films containing ~33 wt % LiTFSI relative to the ONDI-12 block composition and covering a range in ONDI-ph block weight fractions from 0.38 to 070. All spun cast samples have been solvent vapor annealed. The scale bar is 400 nm. The samples include: P-38 (a), P-47 (b), P-48 (c), P-58 (d), P-61 (e), and P-70 (f).
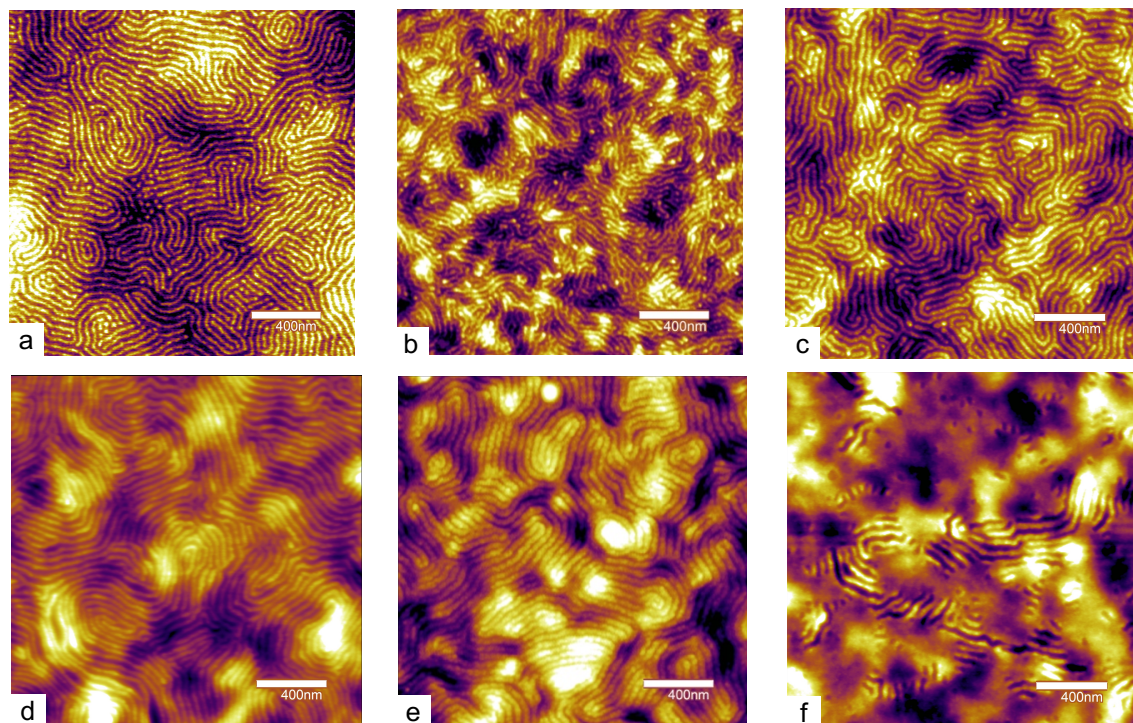
Fig. 6. SAXS data is presented for four polymer samples containing ~39 wt % LiTFSI including P-38 (37 wt %), P-48 (38 wt %), P-58 (38 wt %) , and P-70 (42 wt %). Scattering data is plotted in a Kratky format. The numerical labels on each data set indicate the anticipated q/q* ratios for observed morphology from AFM. P-48 doesn't show scattering peaks suggesting that lamellae are oriented perpendicular to the beam path or the sample is disordered. The former possibility is consistent with AFM data presented in Fig. 5.
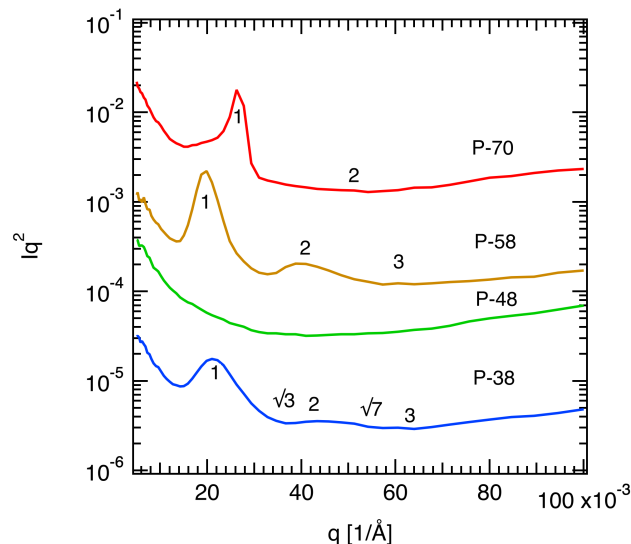

Fig. 7. SAXS data is presented for three samples with salt concentrations near saturation including P-38 (56 wt %), P-48 (50 wt %), and P-58 (46 wt %). The P-70 sample is beyond saturation at these concentrations. Scattering data are plotted in a Kratky format. The numerical labels on each data set indicate possible q/q* ratios.
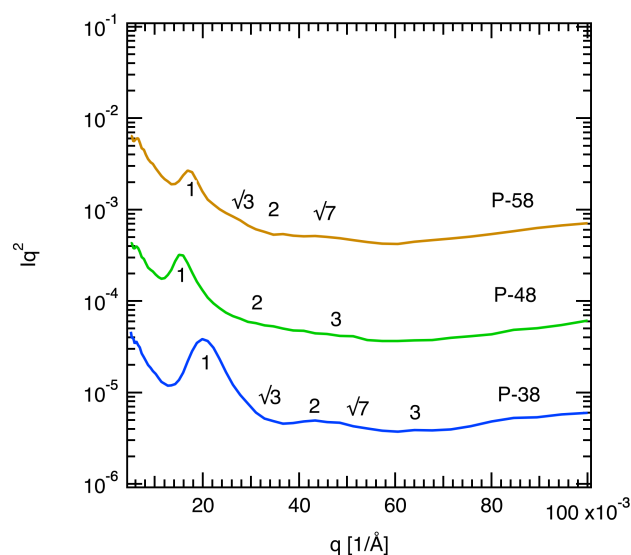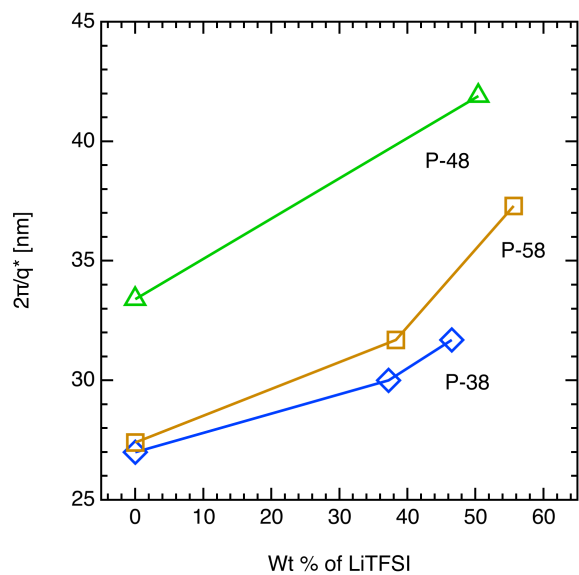

17

Fig. 8. The domain size ($2\pi/q^*$) is plotted versus wt % of LiTFSI for three samples P-38, P-48, and P-58.

References

[1] J.B. Goodenough, Y. Kim, Challenges for Rechargeable Li Batteries, Chemistry of Materials, 22 (2010) 587-603.

[2] V. Etacheri, R. Marom, R. Elazari, G. Salitra, D. Aurbach, Challenges in the development of advanced Li-ion batteries: a review, Energy Environ. Sci., 4 (2011) 3243.

[3] J. Rivnay, S. Inal, A. Salleo, R.M. Owens, M. Berggren, G.G. Malliaras, Organic electrochemical transistors, Nature Reviews Materials, 3 (2018) 17086.

[4] V. Di Noto, S. Lavina, G.A. Giffin, E. Negro, B. Scrosati, Polymer electrolytes: Present, past and future, Electrochimica Acta, 57 (2011) 4-13.

[5] M.D. Tikekar, S. Choudhury, Z. Tu, L.A. Archer, Design principles for electrolytes and interfaces for stable lithium-metal batteries, Nature Energy, 1 (2016) 16114.

[6] D.E. Fenton, J.M. Parker, P.V. Wright, Complexes of alkali metal ions with poly(ethylene oxide), Polymer, 14 (1973) 589.

[7] M. Armand, The history of polymer electrolytes, Solid State Ionics, 69 (1994) 309-319.

[8] K. Hayamizu, E. Akiba, T. Bando, Y. Aihara, 1H, 7Li, and 19F nuclear magnetic resonance and ionic conductivity studies for liquid electrolytes composed of glymes and polyetheneglycol dimethyl ethers of CH3O(CH2CH2O)nCH3 (n=3–50) doped with LiN(SO2CF3)2, The Journal of Chemical Physics, 117 (2002) 5929-5939.

[9] Z. Xue, D. He, X. Xie, Poly(ethylene oxide)-based electrolytes for lithium-ion batteries, Journal of Materials Chemistry A, 3 (2015) 19218-19253.

[10] J. Mindemark, M.J. Lacey, T. Bowden, D. Brandell, Beyond PEO—Alternative host materials for Li+-conducting solid polymer electrolytes, Progress in Polymer Science, 81 (2018) 114-143.

[11] L.D. McIntosh, T. Kubo, T.P. Lodge, Morphology, Modulus, and Conductivity of a Triblock Terpolymer/Ionic Liquid Electrolyte Membrane, Macromolecules, 47 (2014) 1090-1098.

[12] W.-F. Kuan, R. Remy, M.E. Mackay, I.I.I.T.H. Epps, Controlled ionic conductivity via tapered block polymer electrolytes, RSC Adv., 5 (2015) 12597-12604.

[13] K.P. Barteau, M. Wolffs, N.A. Lynd, G.H. Fredrickson, E.J. Kramer, C.J. Hawker, Allyl Glycidyl Ether-Based Polymer Electrolytes for Room Temperature Lithium Batteries, Macromolecules, (2013).

[14] J. Ping, H. Pan, P.P. Hou, M.-Y. Zhang, X. Wang, C. Wang, J. Chen, D. Wu, Z. Shen, X.-H. Fan, Solid Polymer Electrolytes with Excellent High-Temperature Properties Based on Brush Block Copolymers Having Rigid Side Chains, ACS Appl. Mater. Interfaces, 9 (2017) 6130-6137.

[15] K.J. Harry, D.T. Hallinan, D.Y. Parkinson, A.A. MacDowell, N.P. Balsara, Detection of subsurface structures underneath dendrites formed on cycled lithium metal electrodes, Nat Mater, 13 (2014) 69-73.

[16] S.A. Mullin, G.M. Stone, A. Panday, N.P. Balsara, Salt Diffusion Coefficients in Block Copolymer Electrolytes, J. Electrochem. Soc., 158 (2011) A619.

[17] M.A. Ratner, D.F. Shriver, Ion transport in solvent-free polymers, Chemical Reviews, 88 (1988) 109-124.

[18] A.L. Agapov, A.P. Sokolov, Decoupling Ionic Conductivity from Structural Relaxation: A Way to Solid Polymer Electrolytes?, Macromolecules, 44 (2011) 4410-4414.

[19] F. Fan, Y. Wang, A.P. Sokolov, Ionic Transport, Microphase Separation, and Polymer Relaxation in Poly(propylene glycol) and Lithium Perchlorate Mixtures, Macromolecules, 46 (2013) 9380-9389.

[20] Y. Wang, A.P. Sokolov, Design of superionic polymer electrolytes, Current Opinion in Chemical Engineering, 7 (2015) 113-119.

[21] Y. Wang, F. Fan, A.L. Agapov, T. Saito, J. Yang, X. Yu, K. Hong, J. Mays, A.P. Sokolov, Examination of the fundamental relation between ionic transport and segmental relaxation in polymer electrolytes, Polymer, 55 (2014) 4067-4076.

[22] Y. Wang, A.L. Agapov, F. Fan, K. Hong, X. Yu, J. Mays, A.P. Sokolov, Decoupling of Ionic Transport from Segmental Relaxation in Polymer Electrolytes, Physical Review Letters, 108 (2012) 088303.

[23] P. Griffin, A.L. Agapov, A. Kisliuk, X.-G. Sun, S. Dai, V.N. Novikov, A.P. Sokolov, Decoupling charge transport from the structural dynamics in room temperature ionic liquids, The Journal of Chemical Physics, 135 (2011) 114509-114508.

[24] E.W. Stacy, C.P. Gainaru, M. Gobet, Z. Wojnarowska, V. Bocharova, S.G. Greenbaum, A.P. Sokolov, Fundamental Limitations of Ionic Conductivity in Polymerized Ionic Liquids, Macromolecules, (2018).

[25] K. Kunal, C.G. Robertson, S. Pawlus, S.F. Hahn, A.P. Sokolov, Role of Chemical Structure in Fragility of Polymers: A Qualitative Picture, Macromolecules, 41 (2008) 7232-7238.

[26] F. Fan, Y. Wang, T. Hong, M.F. Heres, T. Saito, A.P. Sokolov, Ion Conduction in Polymerized Ionic Liquids with Different Pendant Groups, Macromolecules, 48 (2015) 4461-4470.

[27] M. Adams, V. Richmond, D. Smith, Y. Wang, F. Fan, A.P. Sokolov, D.A. Waldow, Decoupling of ion conductivity from segmental dynamics in oligomeric ethylene oxide functionalized oxanorbornene dicarboximide homopolymers, Polymer, 116 (2017) 218-225.

[28] F.S. Bates, G.H. Fredrickson, Block Copolymers—Designer Soft Materials, Physics Today, 52 (1999) 32-38.

[29] D.R. Sadoway, Block and graft copolymer electrolytes for high-performance, solid-state, lithium batteries, Journal of Power Sources, 129 (2004) 1-3.

[30] P.P. Soo, B. Huang, Y.I. Jang, Y.M. Chiang, D.R. Sadoway, A.M. Mayes, Rubbery Block Copolymer Electrolytes for Solid‐State Rechargeable Lithium Batteries, J. Electrochem. Soc., 146 (1999) 32-37.

[31] R. Yuan, A.A. Teran, I. Gurevitch, S.A. Mullin, N.S. Wanakule, N.P. Balsara, Ionic Conductivity of Low Molecular Weight Block Copolymer Electrolytes, Macromolecules, 46 (2013) 914-921.

[32] E.D. Gomez, A. Panday, E.H. Feng, V. Chen, G.M. Stone, A.M. Minor, C. Kisielowski, K.H. Downing, O. Borodin, G.D. Smith, N.P. Balsara, Effect of Ion Distribution on Conductivity of Block Copolymer Electrolytes, Nano Lett., 9 (2009) 1212-1216.

[33] M. Singh, O. Odusanya, G.M. Wilmes, H.B. Eitouni, E.D. Gomez, A.J. Patel, V.L. Chen, M.J. Park, P. Fragouli, H. Iatrou, N. Hadjichristidis, D. Cookson, N.P. Balsara, Effect of Molecular Weight on the Mechanical and Electrical Properties of Block Copolymer Electrolytes, Macromolecules, 40 (2007) 4578-4585.

[34] K. Timachova, I. Villaluenga, L. Cirrincione, M. Gobet, R. Bhattacharya, X. Jiang, J. Newman, L.A. Madsen, S.G. Greenbaum, N.P. Balsara, Anisotropic Ion Diffusion and Electrochemically Driven Transport in Nanostructured Block Copolymer Electrolytes, J. Phys. Chem. B, 122 (2018) 1537-1544.

[35] W.-S. Young, P.J. Brigandi, T.H. Epps, Crystallization-Induced Lamellar-to-Lamellar Thermal Transition in Salt-Containing Block Copolymer Electrolytes, Macromolecules, 41 (2008) 6276-6279.

[36] O. Oparaji, S. Narayanan, A. Sandy, S. Ramakrishnan, D. Hallinan, Structural Dynamics of Strongly Segregated Block Copolymer Electrolytes, Macromolecules, 51 (2018) 2591-2603.

[37] J. Sun, G.M. Stone, N.P. Balsara, R.N. Zuckermann, Structure–Conductivity Relationship for Peptoid-Based PEO–Mimetic Polymer Electrolytes, Macromolecules, 45 (2012) 5151-5156.

[38] J. Ji, B. Li, W.-H. Zhong, Effects of a Block Copolymer as Multifunctional Fillers on Ionic Conductivity, Mechanical Properties, and Dimensional Stability of Solid Polymer Electrolytes, J. Phys. Chem. B, 114 (2010) 13637-13643.

[39] Y. Gai, D.-P. Song, B.M. Yavitt, J.J. Watkins, Polystyrene-block-poly(ethylene oxide) Bottlebrush Block Copolymer Morphology Transitions: Influence of Side Chain Length and Volume Fraction, Macromolecules, 50 (2017) 1503-1511.

[40] S. Sharick, J. Koski, R.A. Riggleman, K.I. Winey, Isolating the Effect of Molecular Weight on Ion Transport of Non-Ionic Diblock Copolymer/Ionic Liquid Mixtures, Macromolecules, 49 (2016) 2245-2256.

[41] J.S. Harrison, D.A. Waldow, P.A. Cox, R. Giridharagopal, M. Adams, V. Richmond, S.P. Modahl, M.R. Longstaff, R.A. Zhuravlev, D.S. Ginger, Noncontact Imaging of Ion Dynamics in Polymer Electrolytes with Time-Resolved Electrostatic Force Microscopy, ACS Nano, Submitted for publication (2018).

[42] W. Chu, J. Qin, J.J. de Pablo, Ion Distribution in Microphase-Separated Copolymers with Periodic Dielectric Permittivity, Macromolecules, 51 (2018) 1986-1991.

[43] N.S. Wanakule, A. Panday, S.A. Mullin, Ionic Conductivity of Block Copolymer Electrolytes in the Vicinity of Order−Disorder and Order−Order Transitions, Macromolecules, 42 (2009) 5642-5651.